JMEPEG (2011) 20:436–444
DOI: 10.1007/s11665-010-9688-z

1059-9495/$19.00

Effect of Plastic Deformation on the Corrosion Behavior of a Super-Duplex Stainless Steel

Neill C. Renton, Abdu M. Elhoud, and William F. Deans

(Submitted February 8, 2009; in revised form March 18, 2010)

The role of plastic deformation on the corrosion behavior of a 25Cr-7Ni super-duplex stainless steel (SDSS) in a 3.5 wt.% sodium chloride solution at 90 °C was investigated. Different levels of plastic strain between 4 and 16% were applied to solution annealed tensile specimens and the effect on the pitting potential measured using potentiodynamic electrochemical techniques. A nonlinear relationship between the pitting potential and the plastic strain was recorded, with 8 and 16% causing a significant reduction in average E_p, but 4 and 12% causing no significant change when compared with the solution-annealed specimens. The corrosion morphology revealed galvanic interaction between the anodic ferrite and the cathodic austenite causing preferential dissolution of the ferrite. Mixed potential theory and the changing surface areas of the two phases caused by the plastic deformation structures explain the reductions in pitting potential at certain critical plastic strain levels. End-users and manufacturers should evaluate the corrosion behavior of specific cold-worked duplex and SDSSs using their as-produced surface finishes assessing in-service corrosion performance.

Keywords galvanic corrosion, pitting potential, plastic deformation, super-duplex stainless steel

1. Introduction

The duplex grades of stainless steels (DSS) have become increasingly attractive when compared with single-phase austenitic and ferritic grades in many applications as a result of their high strength and corrosion resistance in chloride containing media. The dual-phase ferrite-austenite microstructure of duplex provides a combination of toughness and mechanical strength; while the high chromium, molybdenum, and tungsten content provide a robust surface passive oxide film that provides the material with its corrosion properties making it desirable for many applications in the chemical, nuclear, and petrochemical industries (Ref 1, 2). A material is referred to as a super-duplex stainless steel (SDSS) if its pitting resistance equivalence number (PREN) = Cr% + 3.3(Mo% + 0.5W%) + 16N% is greater than 40 (Ref 2). Despite their excellent material properties, failures of duplex and super-duplex components have occurred in relatively benign environments where environmentally assisted cracks have propagated in regions with high plastic deformation caused by excessive cold-work (Ref 3-5). Plastic deformation is present in most SDSS components as a result of fabrication techniques used in machining, bending, and rolling and its role in the corrosion performance of individual grades is therefore of interest.

Neill C. Renton, Abdu M. Elhoud and **William F. Deans**, School of Engineering, University of Aberdeen, Kings College, Aberdeen AB24 3UE, Scotland, UK. Contact e-mail: n.c.renton@abdn.ac.uk.

At the microstructural level, cold-work introduces a number of plastic deformation structures including dislocation networks, twins, deformation bands, cell structures, and emerging slip steps at the surface (Ref 6). These structural transformations cause considerable changes in the important mechanical and corrosion properties of the material. Of particular concern is the effect the plastic deformation has on the properties of the passive film and the underlying microstructure which can increase the material's susceptibility to localized corrosion attack. The phenomenon has been studied in other grades of stainless steel. The changes in pitting potential of an AISI 316 austenitic stainless steel which was cold-worked in the range 0-40% area reduction demonstrated that from 0-20% area reduction, cold-work increased the pitting potential; however, area reductions beyond 30% reduced the pitting potential when compared with the solution-annealed specimen in higher nitrogen grades (Ref 7). In contrast, a number studies report no beneficial effect of cold-work. Cold-work at 35 and 58% area reduction lowered the critical pitting potential E_p of an AISI 304 austenitic SS in 0.3 wt.% sodium sulfate solution with varying ppm concentrations of sodium chloride (Ref 8). A comprehensive review of studies on single-phase stainless steels shows contrasting reports of both increasing and decreasing E_p with increasing cold-work (Ref 9). The authors go on to describe their detailed study on the effect of cold-work on the various stages of pitting corrosion in an AISI 304 SS demonstrating that in 0.5 M NaCl, the pitting potential reduced with % area reduction. Monotonically decreasing pitting potential with increasing cold-work, in the range 0-60% was also reported in (Ref 10). For austenitic grades of stainless steel, cold-work induced phenomenon such as deformation bands, dislocations, and induced martensite all have a role in the various stages of pitting corrosion, but the effects vary depending on the environment, degree of cold-work, and whether nucleation, growth or repassivation of corrosion pits is studied.

No similar studies of the effect of cold-work on the corrosion resistance of duplex stainless steel grades appear in the literature. However, the types of deformation structures that occur in duplex under strain have been investigated, giving some insight into the potential effect on corrosion resistance. Unlike single-phase grades, the dual-phase structure of DSS and SDSS leads to a nonlinear development of surface structures with increasing cold-work as a result of the different constitutive relations of ferrite and austenite (Ref 11). Atomic force microscopy (AFM) studies confirm the development of a complex surface topography in duplex stainless steel under plastic deformation (Ref 12, 13). The studies revealed that while austenite grains developed a single set of slip bands at the surface inclined with the loading axis, the ferrite developed two separate sets of slip bands; the first caused by plastic deformation in the bulk of the ferrite grain, denoted F1 in (Ref 12); and the second as a result of large scale deformation in adjacent austenite grains where the crystallographic orientations of the bcc-fcc system were well matched (denoted types A1, A2, and F2). The complex surface topography generated by plastic deformation in both the phases will have some effect on the corrosion properties of cold-worked SDSS components, but this has not previously been investigated at the electrochemical level in the literature. It is the aim of this study to investigate the effect of plastic deformation structures on the corrosion resistance of a SDSS alloy in 3.5 wt.% NaCl solution using electrochemical potentiodynamic techniques.

2. Experimental Procedure

The chemical composition of the investigated SDSS in weight percentage (wt.%) was 0.02%C, 24.84%Cr, 6.54%Ni, 3.10%Mo, 2.07%W, 0.47%Cu, 0.45%Mn, 0.34%Si, 0.28%N, remaining Fe. The as-received material was available as a cold-worked tubular which was then solution annealed at 1050 °C for 1 h and water quenched. Cylindrical tensile specimens were then machined from the pipe wall 5 mm in diameter and 100 mm in length. Before straining, specimens were mechanically polished starting with coarse grain emery paper of 240 to 1200 grit followed by a final polish using alumina paste to achieve a mirror-like surface finish. The polished specimens were rinsed with acetone and dried by hot air. Specimens were strained in axial tension to 4, 8, 12, and 16% plastic strain at a constant rate of 0.1 mm/min using an Instron 3200 tensile test machine; a smaller group of specimens were left unstrained (0% strain) as a reference set. The new diameters of the strained specimens were measured to allow the reduction in area to be calculated. A group of example specimens were separated from the main group for metallographic observation using optical and scanning electron microscopy (SEM). Some of the specimens were etched electrochemically in 10 wt.% oxalic acid solution to aid examination. This was achieved by isolating the end of the specimen in an epoxy resin and exposing only the gauge length to the etchant. A 3 V potential difference was then applied for 30 s using a variable power supply and a platinum electrode as the cathodic lead. These specimens were also used to take five separate hardness measurements per strain category using a Vickers indenter. The Hv10 results were averaged and are reported in Table 1.

The electrochemical corrosion behavior of both strained and unstrained specimens was then investigated using potentiodynamic polarization measurements in 3.5 wt.% sodium chloride solution according to ASTM G 5. The electrochemical cell was a conventional three electrode cell comprising the working electrode (specimen); reference silver/silver chloride (Ag/AgCl) electrode; and, a platinum counter electrode. All electrochemical measurements were made at a temperature of 90 °C using a Princeton Potentiostat/Galvanostat (263 A). Before potentiodynamic measurements, the electrodes were immersed in a glass corrosion cell filled with 700 ml of the investigated electrolyte. The open circuit potential became stabilized after 30 min. The potentiodynamic curves were recorded at a potential scan rate of 1 mV/s starting from 100 mV below the open-circuit potential. The potential scan continued while the corrosion current density was monitored. The polarization curves were analysed to determine the breakdown potential at which the current increased monotonically with time beyond 100 μA. A minimum of three specimens per strain level were tested. The experimental set-up is shown in Fig. 1.

3. Results

3.1 Deformation Structures

SEM images of the unstrained and strained specimens are shown in Fig. 2. The uniform surface of the unstrained specimen is shown in Fig. 2(a), with phase boundaries barely visible. In contrast, the deformed surfaces of the 8 and 16% plastic strain specimens are shown in Fig. 2(b) and (c). The images reveal a range of plastic deformation behaviors including deformation bands, slip planes, and phase boundaries between the austenite and the ferrite. The deformation bands in the 16% specimen are more developed both in number and in apparent depth with steps clearly visible.

Table 1 Statistical analysis of the breakdown potential results as a function of plastic prestrain ε_{pl}

Pl-strain ε_{pl}	Area red., %	Ave. Hv10, kgf/mm^2	Sample mean E_p, mV Ag/AgCl	Sample SD, mV Ag/AgCl	COV	Calculated t value				
						0%	4%	8%	12%	16%
0	0	300	643.6	55.61	0.086	0	0.69	**2.57**	1.39	1.73
4	8	335	666.8	45.31	0.068	-	0	**3.19**	0.67	**2.78**
8	12	337	531.0	62.51	0.118	-	-	0	**3.87**	1.73
12	16	357	685.7	42.13	0.061	-	-	-	0	**4.34**
16	18	361	596.4	25.29	0.042	-	-	-	-	0

Note: Bold t values mean the difference in the sample means is significant at the $p = 0.05$ level (95% certain the sample means are from populations with different properties)

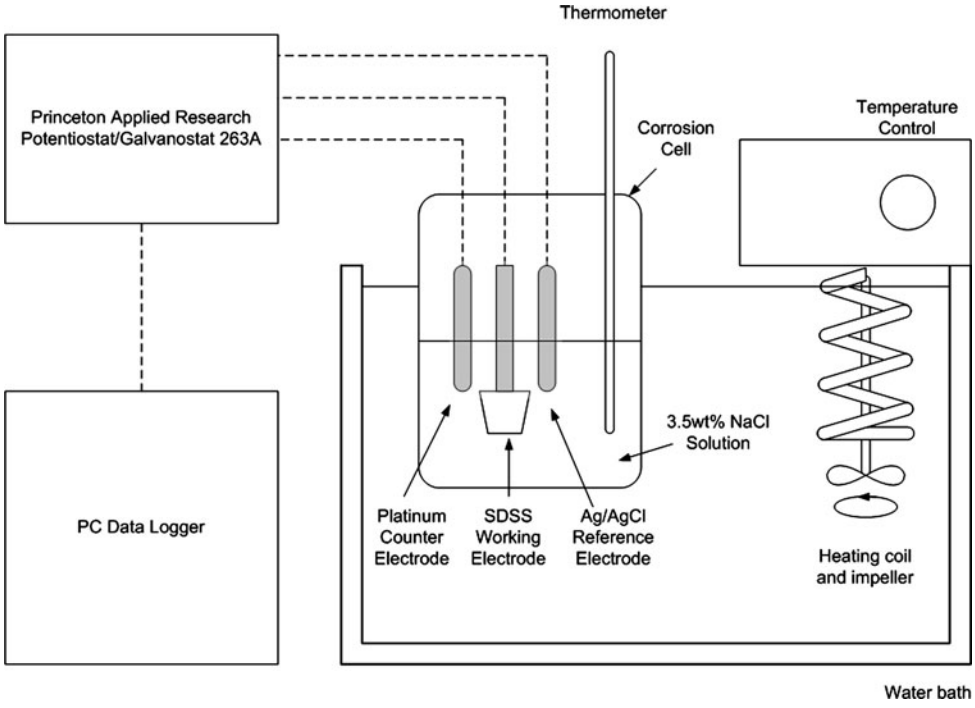

Fig. 1 Experimental set-up for corrosion tests

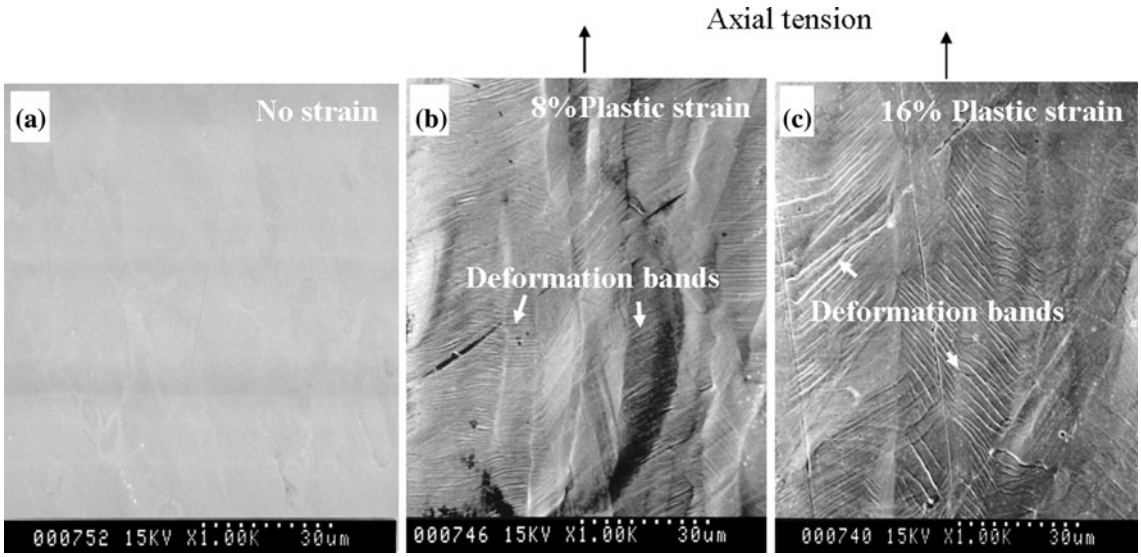

Fig. 2 SEM images of unstrained (0), 8 and 16% plastic strain SDSS specimen surfaces

Polished surfaces were also examined to reveal differences between the plastic deformation behavior of the austenite (γ) and the ferrite (α). The unstrained microstructure is shown in Fig. 3(a), while the microstructure of the specimen strained to 16% plastic strain is shown in Fig. 3(b). There is a clear difference in the ferrite in the 16% specimens with deformation structures visible. Evidence of the complex deformation behavior of ferrite in duplex stainless steels is shown in Fig. 4, where SEM images of an etched surface on the 16% specimen show both type-A and type-F deformation bands of the type reported in (Ref 12, 13). Type-F deformation bands in the center of the ferrite grain can be seen clearly in Fig. 4(a) directly above the 'α', while type-A bands, forming as a result of deformation in the austenite, can be seen at the phase boundary to the left of the 'α'. Example type-A deformation bands are shown in more detail in Fig. 4(b).

3.2 Electrochemical Tests

Example potentiodynamic curves for all levels of plastic strain are shown in Fig. 5(a-e). The curves show the typical polarization behavior of the material with the free corrosion potential; initiation noise; evidence of metastable events prior to the final breakdown of the passive film; and, the monotonic stable increase of current denoting the pitting potential E_p all shown. While there is little difference in the free corrosion

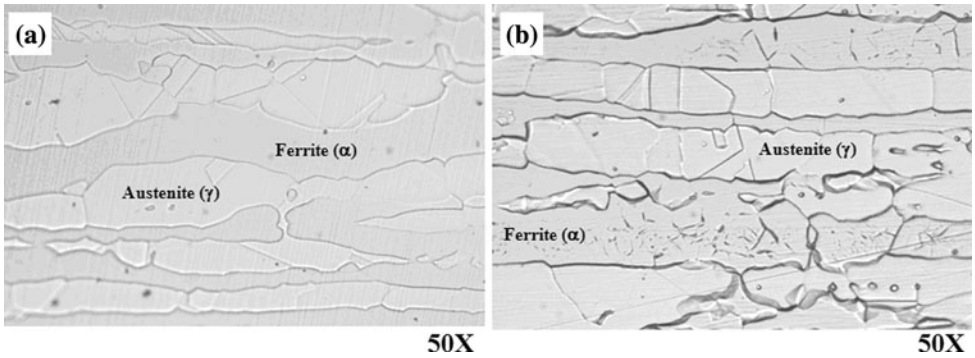

Fig. 3 Microstructure of super duplex alloy after polishing and 10 wt.% oxalic acid etching (a) no plastic deformation, (b) 16% plastic strain

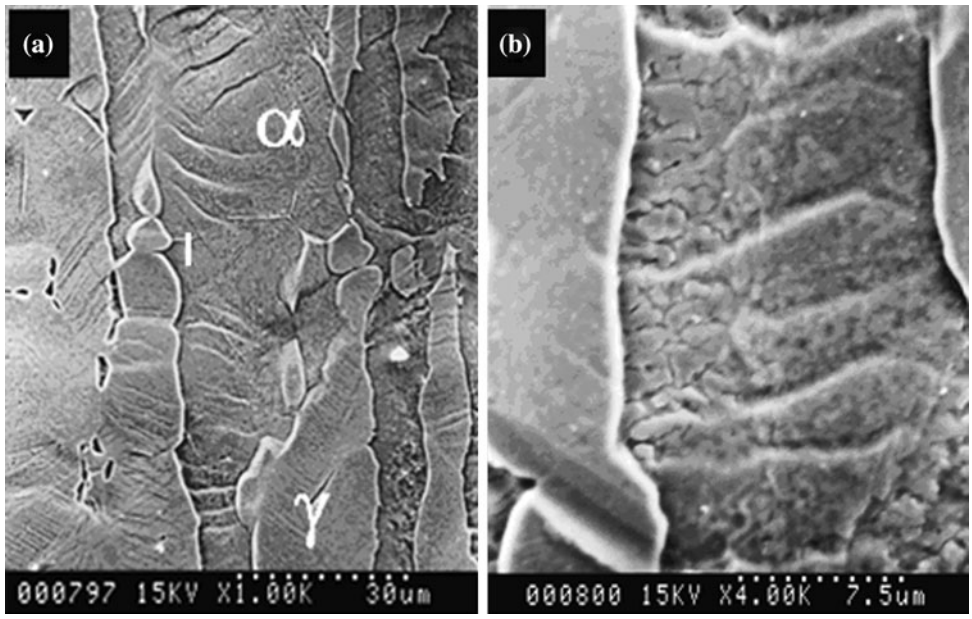

Fig. 4 SEM photographs of 16% plastic strain SDSS specimen after 10 wt.% oxalic acid etching (a) multiple deformation bands in ferrite (b) high magnification at local I

potential between the specimen groups, the potentiodynamic curves show varying pitting potential and metastable events, e.g., the repassivation event at around 400 mV SCE on one of the 8% test curves (Fig. 5c).

The breakdown potential was measured from each test and the results collated and graphed in Fig. 6. The graph shows the expected random variation in E_p within each strain level and the trend of the average value. The sample mean, standard deviation, and coefficient of variation (COV) were calculated for each group of specimens and the Student's t test applied to the results to confirm whether the differences noted between straining levels were actually significant. The t test results demonstrated no significant difference (at $P = 0.05$) between the groups of 0, 4, and 12% specimens, but there was a significant reduction in the breakdown potentials of the 8 and 16% specimens compared with the other three groups. The average E_p dropped to 531 mV (Ag/AgCl) for the 8% specimens and 596 mV for the 16% specimens, compared with the 640-680 mV range of results for the other levels. A summary of the results is contained in Table 1.

3.3 Corrosion Morphology

The corrosion morphology of the 8% plastic strain specimen is shown in Fig. 7(a-c). The figure illustrates an isolated shallow pit 120 × 70 μm in size. The edges of the pit are not uniform, with ferrite grains suffering preferential attack. This preferential dissolution of the ferrite can be seen at higher magnification in Fig. 7(b) and (c) with ferrite (α) and austenite (γ) phases marked. This is a well recorded phenomenon in duplex stainless steels in chloride bearing solutions and is caused by a galvanic couple that forms between the two phases as a result of chemical partitioning; Cr, Mo, W concentrating in ferrite and Ni, N in austenite (Ref 14-17). The high nickel and nitrogen give austenite a more noble potential in chloride solutions making it the cathode to the more negative ferrite (the anode). The result is the sacrificial loss of ferrite seen in the images.

Further evidence of the preferential attack of ferrite is shown in Fig. 8(a-c) which illustrates the corrosion morphology of the 16% plastic strain specimen. The images show further losses in

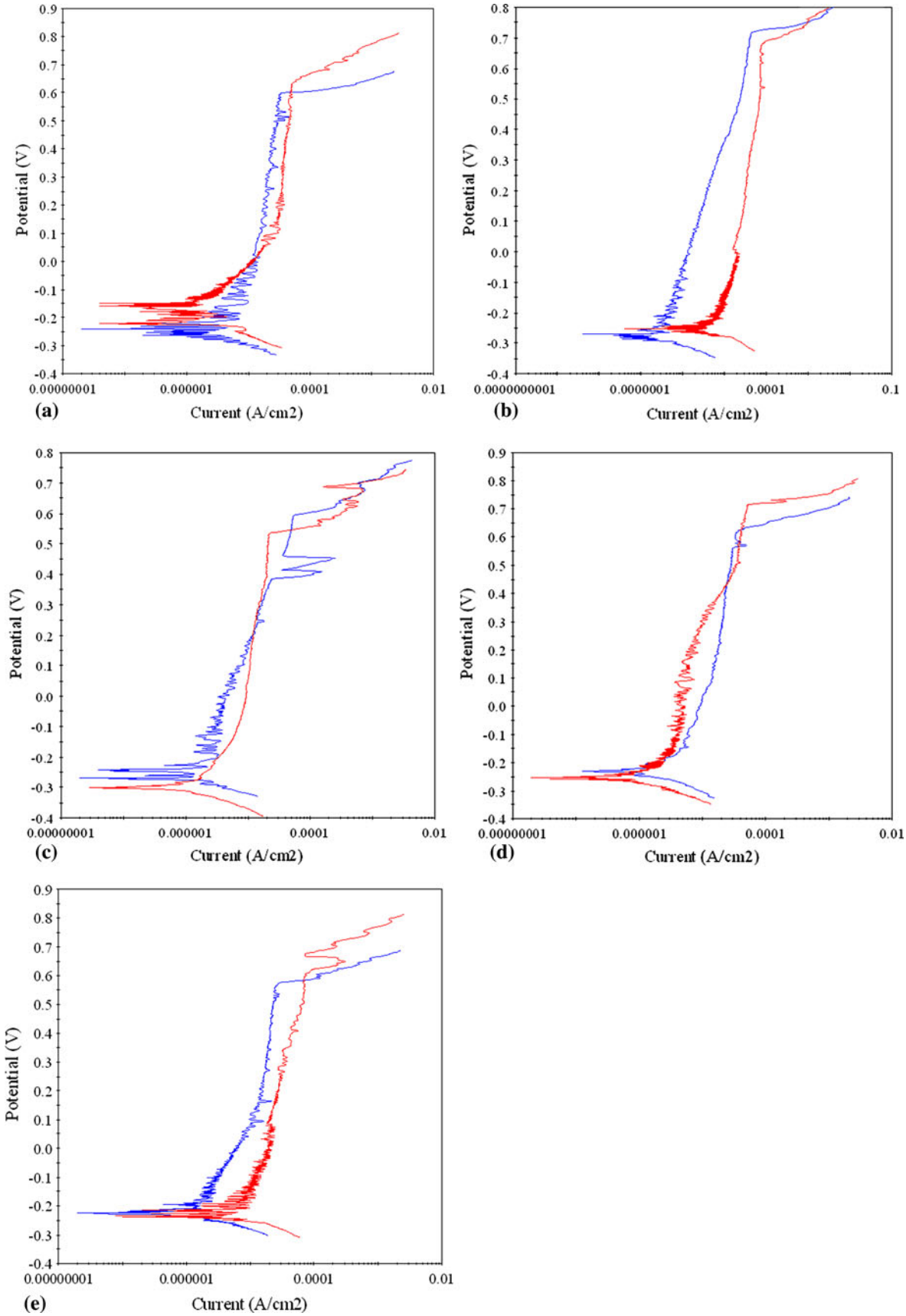

Fig. 5 Example potentiodynamic polarization curves of SDSS alloy cold-worked to different degrees of plastic strain in 3.5 wt.% sodium chloride at 90 °C potentials V Ag/AgCl

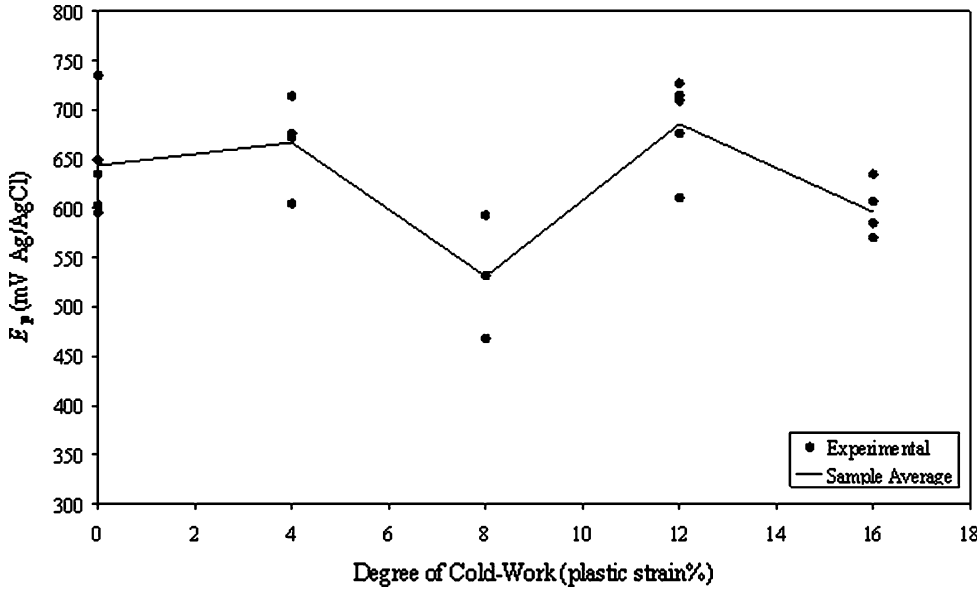

Fig. 6 Effect of cold-work on pitting corrosion potential (E_p) of SDSS alloy in 3.5 wt.% sodium chloride at 90 °C

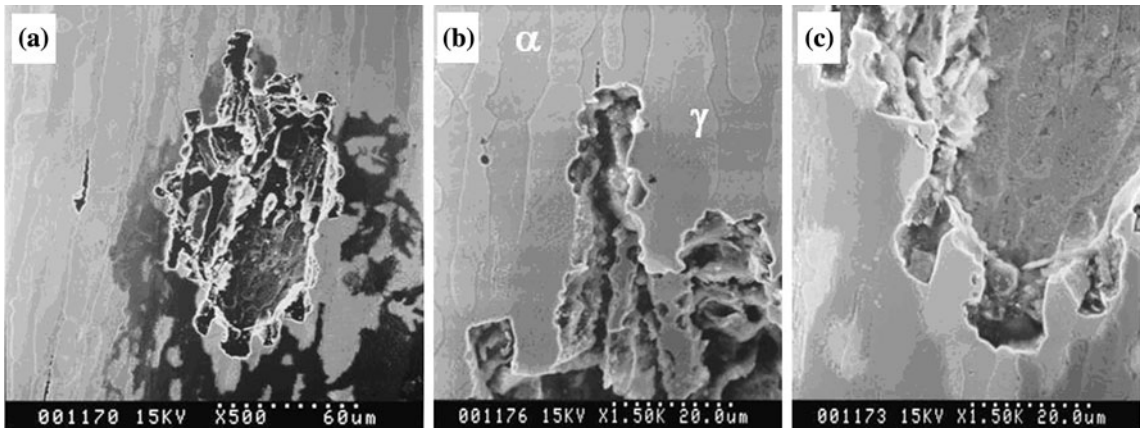

Fig. 7 Pitting corrosion attack on 8% plastic strain SDSS specimen in 3.5 wt.% sodium chloride solution at 90°C; (a) general view for a shallow pit, (b) and (c) higher magnification at the pit propagation edges

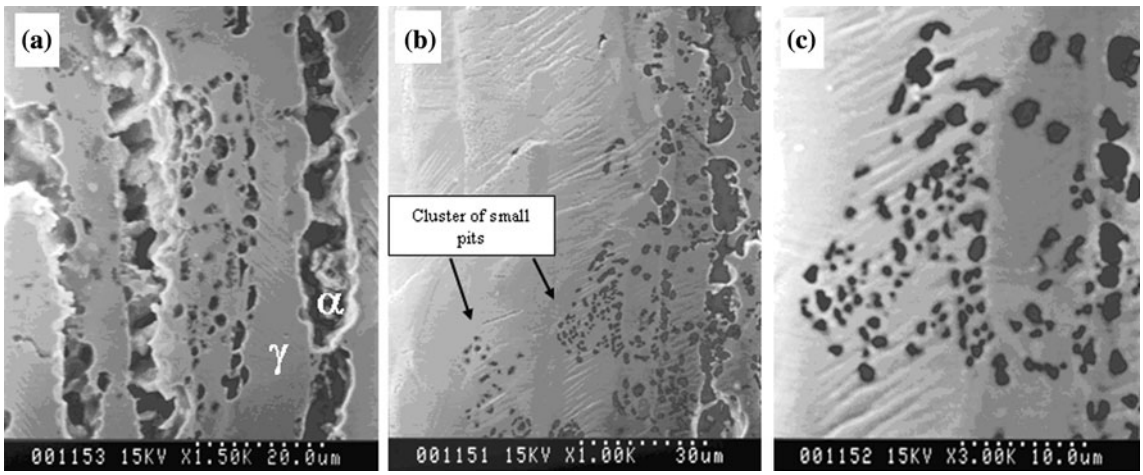

Fig. 8 Pitting corrosion attack on the 16% plastic strain SDSS specimen in 3.5 wt.% sodium chloride solution at 90 °C; (a) general view for severe attack, (b) pit clusters, and (c) higher magnification

the ferrite phase, together with clusters of small pits initiating along the surface grooves of the deformation bands, primarily on the ferrite but also on the austenite phase.

4. Discussion

The results of the experimental programme give an insight into the effects of plastic deformation on the corrosion resistance of the SDSS studied. The SEM images of the strained specimens in Fig. 2 to 4 reveal the expected types of plastic deformation structures reported in (Ref 12, 13), namely a nonlinear development of slip bands in austenite and ferrite with increasing strain. In addition, the ferrite exhibits multiple types of deformation bands including those associated with bulk deformation in the ferrite (F1) and those which have moved across the phase boundary from the austenite (F2, A1, A2). The hardness results, presented in Table 1 and plotted together with the pitting potential results in Fig. 9, confirm the nonlinear behavior quantitatively.

The observed plastic behavior of the duplex stainless steel can be used to interpret the electrochemical results. First, the SDSS results from this study were compared with the single-phase studies reported in (Ref 7-10). It is not possible to report any improvement in corrosion resistance with increasing plastic deformation for the SDSS used in this study. The results are closer to those reported in (Ref 8-10) where small reductions in E_p occurred at cold-work levels below 20% area reduction. However, there are also some notable differences from the single-phase studies. At 8 and 16% plastic strain there is a significant reduction in the pitting potential that was not evidenced at the other strain rates. Similar changes to the corrosion behavior of SDSS at different degrees of cold-work, with reductions at apparently critical plastic strains, have been reported elsewhere (Ref 18). This change in corrosion behavior is related to the complex deformation of austenite and ferrite within the duplex microstructure. The role of the deformation structures that form on the external surface of the strained specimens are of interest. The results in Fig. 2 to 4 show the deformation structures increase with strain, confirmed by the AFM studies in (Ref 12, 13) and by the hardness results in Fig. 9. As a result, the reduction in corrosion resistance at 8 and 16% plastic strain cannot be explained by deformation changes alone.

Changes in the surface topography are one possible explanation. As deformation develops, the slip bands produce geometric shapes capable of acting as diffusion inhibitors at the initiation stage of pitting corrosion (Ref 19). However, while this effect is present, as evidenced by pit initiation sites following the deformation bands in Fig. 8(c), it should have produced a reduction in pitting potential with increasing strain as the surface roughness increased. In addition to the effect of topographical changes, plastic deformation increases the number of suitable initiation sites (Ref 19). The SEM images confirm that deformation bands increased with increasing strain so again the effect should have led to decreasing pitting potentials with increasing strain as the number of sites increased (Ref 8-10). A reduction in pitting potential with increasing strain is however not what is observed in Fig. 9; a different mechanism must be involved in the development of pitting corrosion in the cold-worked duplex.

The preferential dissolution of the ferrite phase shown in Fig. 7 and 8 is of interest. The volume fraction of ferrite in a duplex stainless steel was shown to have a direct effect on the strength of the galvanic couple that forms between the two phases and hence the dissolution rate of ferrite which was preferentially attacked (Ref 15). Further detailed measurement of the effect in a more recent study confirmed the difference in free corrosion potential between the anodic ferrite and the cathodic austenite in chloride-bearing solutions is approximately 25 mV relative to a standard calomel electrode, while the galvanic current flowing from the ferrite to the austenite was 0.1-0.13 mA (Ref 16). The electrochemical interaction between the two phases, and the sacrificial consumption of ferrite by the austenite in chloride-bearing solutions, is then controlled by their relative surface areas. In this study, the initially polished specimen surfaces moved from 2-dimensional radial planes, to 3-dimensional topographies as the deformation bands developed on both the phases during straining prior to the corrosion

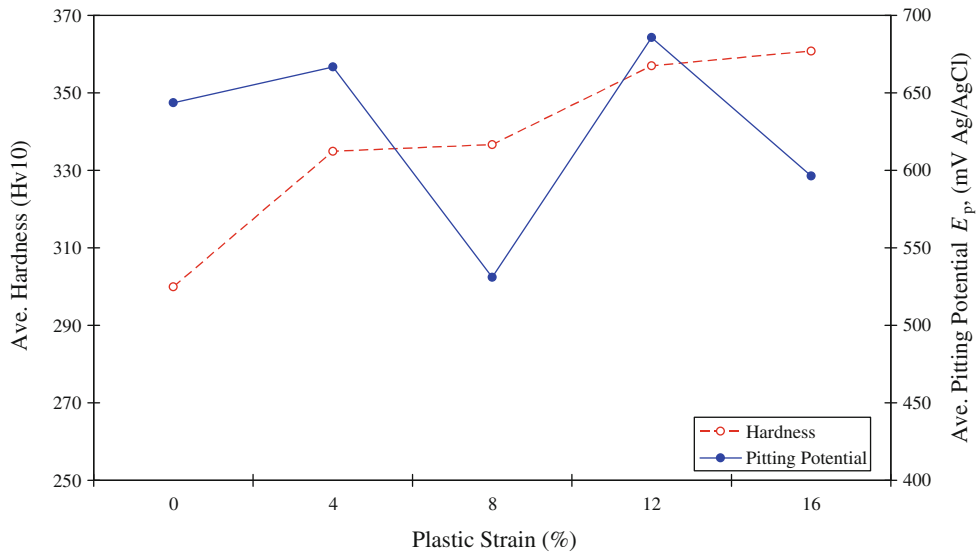

Fig. 9 The effect of cold-work on the corrosion resistance of SDSS

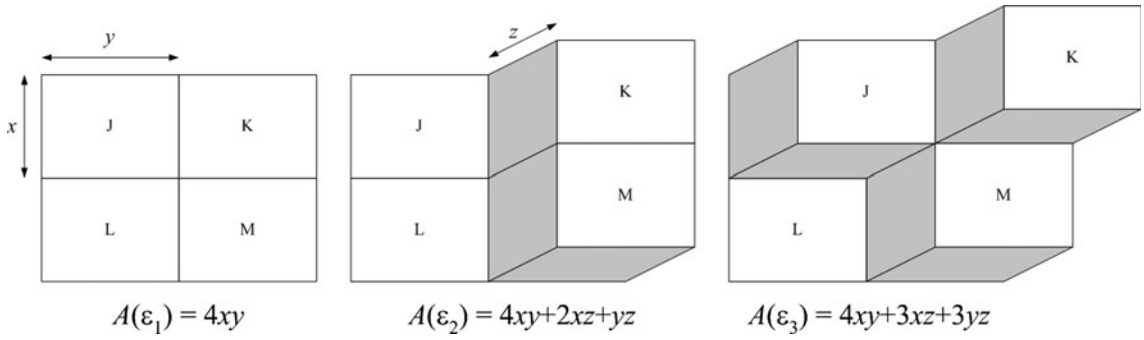

Fig. 10 Development of deformation bands in one of the phases of an SDSS and their effect on the exposed surface area

tests. The deformation structures that form, and hence the topographies, develop differently in the ferrite and austenite phases with increasing strain. As a result, the exposed surface areas of the two phases (anode and cathode) are changing relative to one another as plastic strain increases. The effect in one phase is represented in Fig. 10, showing how the initial surface area at plastic strain level ε_1, denoted $A(\varepsilon_1)$, is constructed of four rectangles JKLM of sides xy to give $A(\varepsilon_1)$ as $4xy$. As the plastic strain increases $\varepsilon_1 < \varepsilon_2 < \varepsilon_3$, the visible surface areas $A(\varepsilon_2)$ and $A(\varepsilon_3)$ increase, as a result of deformation bands, to $4xy + 2xz + yz$ and $4xy + 3xz + 3yz$, respectively. Classical mixed potential theory can be used to show that galvanic corrosion current density (and hence corrosion rate) directly proportional to the anode/cathode area ratio such that (Ref 15):

$$\log\left[i_a^{\alpha}\right] = M \log\left[\frac{(1-f)}{f}\right] + N \qquad \text{(Eq 1)}$$

where M is a function of the gradients of the potential-current relationships for austenite and ferrite, found to be approximately 0.75 for all stainless steels; N is function of the free corrosion potentials of the two phases which change with chemical composition; f is the volume fraction of ferrite; and, i_a^{α} is the galvanic corrosion current density of the ferrite (Amp/cm^2) (Ref 15). The expression in Eq 1 can be developed for the case when the phase areas are changing with increasing plastic deformation structures. First, the area fraction of a phase is equivalent to its volume fraction. If we assume that the austenite and ferrite phases make up 100% of the material volume then $A\gamma + A\alpha = 1.0$. Since the exposed surface areas of both phases are functions of strain, $A_\gamma(\varepsilon)$ and $A_\alpha(\varepsilon)$, then Eq 1 can be restated as:

$$\log\left[i_a^{\alpha}(\varepsilon)\right] = 0.75 \log\left[\frac{A_\gamma(\varepsilon)}{A_\alpha(\varepsilon)}\right] + N \qquad \text{(Eq 2)}$$

It follows directly that a changing surface area ratio must result in a change to the galvanic current flowing between the austenite and the ferrite locally (Ref 15). The plastic deformation behavior of austenite and ferrite reported here in Fig. 2 to 4 confirms that ferrite experiences multiple systems of deformation bands through interaction with surrounding austenite grains. The nonlinear development of the deformation bands in both the phases with increasing plastic strain is quantified in the results of Fig 7 of (Ref 12), which presents a simple count of the number of deformation bands in austenite (n_γ) together with the number of type-A and type-F deformation bands in ferrite (n_α). A simple ratio between the two sets of numbers presented in (Ref 12) gives a rough idea of how the surface areas of ferrite $A_\alpha(\varepsilon)$ and austenite $A_\gamma(\varepsilon)$ grains in a DSS change with increasing plastic strain. The ratio of deformation band numbers n_γ/n_α for plastic strains of 0.2, 0.7, 1.15, and 1.18% are approximately 8.00, 2.63, 3.21, and 2.23, respectively, showing that even for these small plastic strains, the relative areas of austenite and ferrite grains are changing with respect to each other in a nonlinear fashion with increasing strain (Ref 12). The rate of change of surface areas with plastic strain for both the phases is then unequal:

$$\frac{dA_\gamma(\varepsilon)}{d\varepsilon} \neq \frac{dA_\alpha(\varepsilon)}{d\varepsilon} \qquad \text{(Eq 3)}$$

From Eq 2 and 3, increasing plastic strain by $d\varepsilon$ means that the galvanic current density must change in a nonlinear fashion with increasing plastic strain. The breakdown of the weaker ferrite at lower potentials for 8 and 16% plastic strain is then best explained by the changing surface areas of austenite and ferrite caused by the complex development of deformation bands in both the phases during the cold-working process in duplex stainless steels. Future study will focus on quantifying the relationship between austenite and ferrite at different levels of plastic strain experimentally using advanced electrochemical methods to observe changes in localized galvanic current at the micro-level between individual ferrite and austenite grain systems as a function of plastic strain.

5. Conclusions

The effect of plastic deformation on the corrosion resistance of a cold-work SDSS was investigated in 3.5 wt.% NaCl solution at 90 °C. The results demonstrated that:

1. Cold-work of 4-16% plastic strain has no significantly beneficial effect on the pitting potential of a solution-annealed SDSS surface and can have a detrimental effect at certain critical levels of 8 and 16%.
2. Plastic deformation of austenite and ferrite develops in a nonlinear fashion with increasing plastic strain. Ferrite develops multiple types of deformation bands through an interaction with local austenite grains.
3. The nonlinear relationship between the plastic strain and the pitting potential of cold-worked SDSSs is caused by the changing surface area ratio of the cathodic-austenite and anodic-ferrite which in turn directly affects the strength of the galvanic couple between the two phases.

4. Manufacturers and end-users of cold-worked SDSS grades should take steps to assess the effect of specific plastic strains on corrosion resistance.

References

1. S.S.M. Tavares, V.F. Terra, J.M. Parada, and M.P. Cindra Fonseca, Influence of the Microstructure on the Toughness of a Duplex Stainless Steel UNS S31803, *J. Mater. Sci.*, 2005, **40**, p 145–154
2. J.O. Nilsson, Super Duplex Stainless Steel, *Mater. Sci. Technol.*, 1992, **8**, p 685–700
3. A.W. Glass. Research Report 409: High Pressure, High Temperature Developments in the United Kingdom Continental Shelf. Health and Safety Executive, 2005
4. C. Coussement and D. Fruytier, An Industrial Application of Duplex Stainless Steel in the Petrochemical Industry: A Case Study, Failure Analysis and Subsequent Investigations, *Duplex Stainless Steels* '91, Vol. 1, J. Charles and S. Bernhardsson, Eds., Les editions de physique, 1991, p 521–529
5. I.M. Hannah and D. Seymour, Shearwater super-duplex tubing failure investigation *NACE-International Corrosion Conference Series*, 2006, paper 77053
6. U. Kamachi Mudali, P. Shankar, S. Ningshen, Sanjay Rai, and R.K. Dayal, Pitting corrosion studies on cold worked nitrogen-bearing austenitic stainless steels, *7th International Symposium on Electrochemical Methods in Corrosion Research*, 2000, Paper 125, *Proceedings of EMCR2000*
7. U. Kamachi Mudali, P. Shankar, S. Ningshen, R.K. Dayal, H.S. Khatak, and B. Raj, On the Pitting Corrosion Resistance of Nitrogen Alloyed Cold Worked Austenitic Stainless Steels, *Corros. Sci.*, 2002, **44**(10), p 2183–2198
8. A. Barbucci, G. Cerisola, and P.L. Cabot, Effect of Cold Working in the Passive Behaviour of 304 Stainless Steel in Sulfate Media, *J. Electrochem. Soc.*, 2002, **149**(12), p B534–B542
9. L. Peguet, B. Malki, and B. Barouxtitle, Influence of Cold Working on the Pitting Corrosion Resistance of Stainless Steels, *Corros. Sci.*, 2007, **49**(4), p 1933–1948
10. Y. Fu, X. Wu, E. Han, W. Ke, K. Yang, and Z. Jiang, Influence of Cold Work on Pitting Corrosion Behaviour of a High Nitrogen Stainless Steel, *J. Electrochem. Soc.*, 2008, **155**(8), p C455–C463
11. J. Johansson and M. Oden, Load Sharing Between Austenite and Ferrite in a Duplex Stainless Steel During Cyclic Loading, *Metall. Mater. Trans. A*, 2000, **31A**, p 1557–1570
12. I. Serre, D. Salazar, and J.-B. Vogt, Atomic Force Microscopy Investigation of Surface Relief in Individual Phases of Deformed Duplex Stainless Steel, *Mater. Sci. Eng. A*, 2008, **492**, p 428–433
13. S. Fréchard, F. Martin, C. Clément, and J. Cousty, AFM and EBSD Combined Studies of Plastic Deformation in a Duplex Stainless Steel, *Mater. Sci. Eng. A*, 2006, **418**, p 312–319
14. S. Bernhardsson. The Corrosion Resistance of Duplex Stainless Steels, *Duplex Stainless Steels '91*, Vol. 1, J. Charles and S. Bernhardsson, Eds., Les editions de physique, 1991, p 185–210
15. Y.-H. Yau and M.A. Streicher, Galvanic Corrosion of Duplex FeCr-10%Ni Alloys in Reducing Acids, *Corrosion*, 1987, **43**(6), p 366–373
16. W.-T. Tsai and J.-R. Chen, Galvanic Corrosion Between the Constituent Phases in Duplex Stainless Steel, *Corros. Sci.*, 2007, **29**, p 3659–3668
17. M. Femenia, C. Canalias, J. Pan, and C. Leygraf, Scanning Kelvin Probe Force Microscopy and Magnetic Force Microscopy for Characterization of Duplex Stainless Steels, *J. Electrochem. Soc.*, 2003, **150**(6), p B274–B281
18. K. Takizawa, Y. Shimizu, E. Yoneda, S. Hokoto, and I. Tamura, Effect of Cold Work and Heat Treatment on Stress Corrosion Cracking Behaviour of Duplex Stainless Steel, *Trans. Iron Steel Inst. Jpn.*, 1979, **65**(6), p 617–626 (in Japanese)
19. P.C. Pistorius and G.T. Burstein, Metastable Pitting Corrosion of Stainless Steel and the Transition to Stability, *Philos. Trans. Phys. Sci. Eng.*, 1992, **341**(1662), p 531–559